Acta Med. Okayama, 2021
Vol. 75, No. 2, pp. 139–145

Acta Medica Okayama
http://escholarship.lib.okayama-u.ac.jp/amo/

Original Article

Evaluation of the Imaging Process for a Novel Subtraction Method Using Apparent Diffusion Coefficient Values

Kentaro Hamada[a], Masahiro Kuroda[a]*, Yuuki Yoshimura[a,b], Abdullah Khasawneh[c], Majd Barham[c], Nouha Tekiki[c], Irfan Sugianto[c,d], Babatunde O. Bamgbose[c,e], Kohei Konishi[a], Kohei Sugimoto[a], Hinata Ishizaka[a], Akira Kurozumi[f], Toshi Matsushita[f], Seiichiro Ohno[f], Susumu Kanazawa[g], and Junichi Asaumi[c]

[a]Radiological Technology, Graduate School of Health Sciences, Okayama University, [c]Department of Oral and Maxillofacial Radiology, [f]Central Division of Radiology, Okayama University Hospital, [g]Department of Radiology, Okayama University Graduate School of Medicine, Dentistry and Pharmaceutical Sciences, Okayama 700-8558, Japan, [b]Radiology Diagnosis, Okayama Saiseikai General Hospital, Okayama 700-8511, Japan, [d]Department of Oral Radiology, Faculty of Dentistry, Hasanuddin University, Makassar, Indonesia, [e]Department of Oral Diagnostic Sciences, Faculty of Dentistry, Bayero University Kano, Kano, Nigeria

Diffusion-weighted imaging may be used to obtain the apparent diffusion coefficient (ADC), which aids the diagnosis of cerebral infarction and tumors. An ADC reflects elements of free diffusion. Diffusion kurtosis imaging (DKI) has attracted attention as a restricted diffusion imaging technique. The ADC subtraction method (ASM) was developed to visualize restricted diffusion with high resolution by using two ADC maps taken with different diffusion times. We conducted the present study to provide a bridge between the reported basic ASM research and clinical research. We developed new imaging software for clinical use and evaluated its performance herein. This software performs the imaging process automatically and continuously at the pixel level, using ImageJ software. The new software uses a macro or a plugin which is compatible with various operating systems via a Java Virtual Machine. We tested the new imaging software's performance by using a Jurkat cell bio-phantom, and the statistical evaluation of the performance clarified that the ASM values of 99.98% of the pixels in the bio-phantom and physiological saline were calculated accurately ($p < 0.001$). The new software may serve as a useful tool for future clinical applications and restricted diffusion imaging research.

Key words: apparent diffusion coefficient, ADC subtraction method, restricted diffusion, ImageJ, plugin

Diffusion-weighted imaging (DWI) is an imaging technique that measures the movement of hydrogen atoms, and it can thus be used to investigate the movement of water molecules present in large quantities in the human body. In DWI, the apparent diffusion coefficient (ADC) maps are useful for clinical applications and reflects elements of free diffusion [1-4]. Diffusion kurtosis imaging (DKI) is a restrictive diffusion imaging technique that has been reported to visualize lesions more sensitively than ADC maps [5,6]. The ADC subtraction method (ASM) is a new method that can visualize restricted diffusion [7]. Since ASM values correlate with the mean kurtosis values calculated by DKI, ASM values might be an index of restricted diffusion [7].

The new ASM method that we developed [7] has a limitation in that there has been no imaging technology

Received March 10, 2020; accepted October 19, 2020.
*Corresponding author. Phone: +81-86-235-6873; Fax: +81-86-235-6873
E-mail: kurodamd@cc.okayama-u.ac.jp (M. Kuroda)

Conflict of Interest Disclosures: No potential conflict of interest relevant to this article was reported.

for clinical applications based on its principles until now. We conducted the present study to provide a bridge between the previously reported principles and clinical research; we developed an image processing software program that calculates images on a pixel-by-pixel bases. We evaluated the software program's performance herein by using verification images of a Jurkat cell bio-phantom. We also examined and evaluated the accuracy of the bit conversion used in the calculation process of the software.

Materials and Methods

Phantom. We used Jurkat cells purchased from Bio Resource Center (Tsukuba, Japan) for the bio-phantom. For cell cultures, we added 10% fetal bovine serum (Filtron, Victoria, Australia) and 1% penicillin-streptomycin-neomycin (Gibco; Thermo Fisher Scientific, Waltham, MA, USA) to RPMI-1640 medium (pH 7.4; Gibco; Thermo Fisher Scientific). The incubation was performed at 37°C with 5% CO_2. The number of cells with a diameter > 8 μm was counted with an electric cell counter (Coulter Electronics, Luton, UK) prior to the preparation of the bio-phantom, since the diameter of the majority of Jurkat cells is > 8 μm, with the mean dia. of 9.6 μm [8].

The Jurkat cells were encapsulated into micro-cuvettes (#halbmikro 1.5 ml; Greiner Labortechnik Manufacturing, Düsseldorf, Germany) as bio-phantoms. Briefly, once the cell number had been determined, the cell solution was concentrated to approx. 0.89 ml, placed in a micro-cuvette, and centrifuged at 161 *g* for 5 min. The supernatant was then removed and the cell density was adjusted to approx. $1-8\times10^8$ cells/ml. After treatment, the cells were enclosed in gellan gum (P-8169; Sigma-Aldrich; Merck, Darmstadt, Germany). The bio-phantom of 7.41×10^8 cells/ml was prepared as a pellet-like high-cell-density phantom. The bio-phantom was enclosed in a phantom container (9.5 cm long, 14 cm wide, 7 cm high) [9]. The interior of the container was filled with physiological saline (0.9% NaCl).

Magnetic resonance imaging. For magnetic resonance imaging (MRI) of bio-phantoms, a phantom container was installed in a bio-phantom heating device that we constructed, which was formed of ethylene-vinyl acetate copolymer and was connected to a circulating thermostatic chamber (Thermo-Mate BF-41; Yamato Scientific Co., Tokyo). The temperature of the bio-phantom was adjusted to approx. 37°C, which is similar to the normal human body temperature. For real-time phantom temperature measurements, an optical fiber thermometer (Fluoroptic™ m3300, Luxtron Co., Santa Clara, CA, USA) was installed in the micro-cuvette during the MRI examination.

A 3.0T MRI scanner (MAGNETOM Prisma VE11C; Siemens, Munich, Germany), which has a 20-channel head/neck coil, was used for imaging. The readout segmentation of long variable echo-trains (RESOLVE) was used for the DWI to eliminate image distortions at the pixel level during subtraction. The RESOLVE-basic and RESOLVE-modify sequences are presented in Table 1. In RESOLVE-modify, a b-value of 10,000 is added to extend the effective diffusion time.

With these 2 sequences, 2 types of ADC maps with different diffusion times were generated as 16-bit images. The first ADC map with an effective diffusion time of 39.3 msec was generated using RESOLVE-basic, and the second ADC map with an effective diffusion time of 46.0 msec was generated using RESOLVE-modify with b-values of 0, 500 and 1,000. The RESOLVE-modify sequence with the b-value of 10,000 was not used to create the second ADC map.

The development of the new ASM imaging software. ASM values are calculated using Eq. (1) [7]:

$$\mathrm{ASM} = |\text{1st ADC} - \text{2nd ADC}|/(\text{1st ADC})^3 \quad (1)$$

where '1st ADC' and '2nd ADC' are the ADC values in each pixel of the first and second ADC maps, respectively. In the present study, we calculated the ASM values on a pixel-by-pixel basis with Eq. (1) by using the following method, and we developed the software pro-

Table 1 Imaging conditions of the apparent diffusion coefficient (ADC) subtraction method

Parameters	RESOLVE-basic	RESOLVE-modify
Effective diffusion time (msec)	39.3	46.0
b-value (sec/mm^2)	0, 500, 1,000	0, 500, 1,000, 10,000
Δ (msec)	41.2	51.2
δ (msec)	5.6	15.6
TR (msec)	8,000	8,000
TE (msec)	86	106
ES (msec)	0.56	0.56
FOV (mm)	120	120
Matrix	224 × 224	224 × 224

RESOLVE, readout segmentation of long variable echo-trains; Δ, motion probing gradient (MPG) pulse spacing; δ, MPG pulse duration; TR, repetition time; TE, echo time; ES, echo space; FOV, field of view.

gram to create ASM images.

ImageJ (ver. 1.51j8; U.S. National Institutes of Health, Bethesda, MD, USA) was used to develop the new ASM imaging software program. A flowchart representing the inter-image calculations based on the ASM principle is presented in Fig. 1. The first and second ADC maps were created as the 16-bit images. In Eq. (1), the difference in the ADC value is divided by the 1st ADC, but the difference is small, and the value divided by the 1st ADC is a value below the decimal point. In 16-bit gradation of an ADC map, the decimal point cannot be handled and only integers can be handled, and thus the calculation of ASM values becomes inaccurate. The 32-bit gradation of an ADC map has two advantages: it can handle values below the decimal point, and the maximum limit is greater than the maximum of 16-bit gradation, which is 65,535. We therefore converted the gradation of the first and second ADC maps from 16 to 32 bits.

Each pixel of the 2 maps was multiplied by the constant 10^{11} to make the difference larger. We obtained the constant 10^{11} from preliminary experiments (data not shown). Next, the absolute difference value between the resulting two ADC maps was calculated pixel by pixel. The absolute difference value was divided by the ADC value of the first 32-bit ADC map three times. This process aimed to decrease the large standard deviations often associated with large ADC values in the ADC maps. Since general medical images are 16-bit images, we converted the gradation from 32 bits to 16 bits. Finally, we created an ASM software program using a macro so that the described calculation was executed automatically and continuously using ImageJ software. We all created an ASM program using a plugin to follow the rules of the programming language Java. The plugin is compatible with various operating systems that use a Java Virtual Machine.

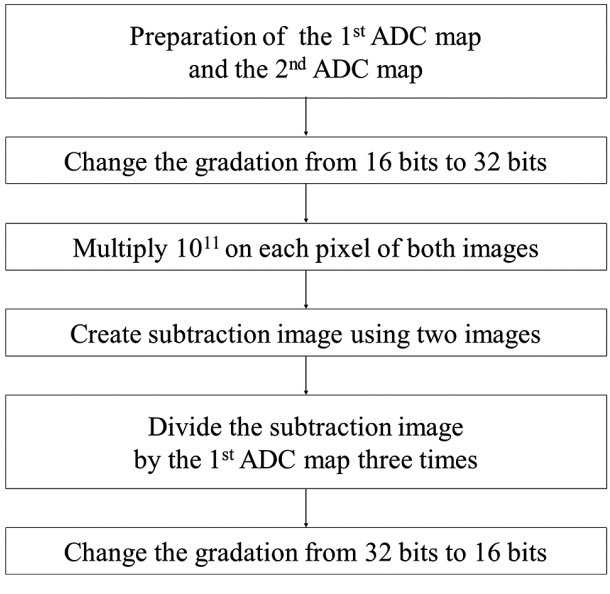

Fig. 1 A flowchart of the calculations based on the apparent diffusion coefficient (ADC) subtraction method used in the present study.

Evaluation of the images in each imaging process for the ASM calculation. We extracted the images of each ASM calculation process in the new software and compared the image changes by visual evaluation and using histograms. The conversion process from 32 bits to 16 bits was verified for the following reasons. The maximum signal value of 32-bit images is 4,294,967,295 which is more than that of 16-bit images, *i.e.*, 65,535 [10]. In addition, the 32-bit image has unique pixel values such as infinity and Not a Number (NaN). In the 32-bit images, pixels with a signal value >65,535, infinity, and NaN may be problematic during the conversion process from 32 to 16 bits in ImageJ. When converting from 32 to 16 bits, the pixel values of >65,535 and infinity become 65,535 (the maximum signal value of 16-bit images), and the pixel value of NaN becomes 0.

To evaluate these issues, we identified and evaluated the appearance ratios of these pixel values in the ASM process of calculating in 32 bits. A region of interest (ROI) was set for each of 'bio-phantom and physiological saline' and 'plastic and air.' The ratios of the number of pixels to the number of all pixels in each ROI were calculated for a signal value >65,535, infinity, and NaN. The significance of differences in the ratios was tested using Fisher's exact test (BellCurve for Excel, Social Survey Research Information Co., Tokyo). Probability (p) values <0.05 were accepted as significant.

Results

Comparison of the images in each imaging process for the ASM calculation. ImageJ software was used to execute the calculations based on the principles of ASM. The images produced for the bio-phantom and physiological saline following important steps of the calculation process are presented in Fig. 2. The bio-

phantom was used as the validation sample (Fig. 2A). The first ADC maps produced for the bio-phantom and physiological saline are shown in Fig. 2B. This ADC map was calculated using DWI taken with the RESOLVE-basic sequence (Table 1).

The second ADC maps (Fig. 2C) of the same bio-phantom and physiological saline were calculated using DWI taken with the RESOLVE-modify sequence (Table 1). There was no apparent difference between the two ADC maps. The gradation of the first and second ADC maps was converted from 16 to 32 bits. Each pixel of the first and second ADC maps was multiplied by 10^{11}. The image of the absolute difference value between the first and second ADC maps, which were converted from 16 to 32 bits and multiplied by 10^{11}, was created (Fig. 2D). An image was subsequently obtained by dividing the image of the absolute difference value (Fig. 2D) by the first 32-bit ADC map 3 times. The gradation of this image was converted from 32 to 16 bits in order to maintain the signal value under the maximum signal value of the 16-bit image (65,535). Figure 2E presents the resultant ASM images of the bio-phantom and physiological saline. These results clarified that the ASM imaging software correctly visualized images on a pixel-by-pixel basis according to the ASM calculation principle.

Verification in the conversion process from 32 bits to 16 bits. Figure 3A shows the first ADC map, in which the pixels with a signal value 0 and the other pixels are indicated as white and black, respectively.

The ratios of infinity (Fig. 3B), NaN (Fig. 3C), and a signal value > 65,535 (Fig. 3D) in the ROI of 'bio-phantom and physiological saline,' the pixel number of which was 6,598 were 0%, 0%, and 0.02%, respectively (Table 2). The ratios of infinity (Fig. 3B), NaN (Fig. 3C), and a signal value > 65,535 (Fig. 3D) in the ROI of 'plastic and air,' the pixel number of which was 3,203 were 0.97%, 0.53%, and 9.33%, respectively (Table 2). These ratios in the ROI of 'bio-phantom and physiological saline' were significantly lower than those in the ROI of 'plastic and air' for infinity (Fig. 3B), NaN (Fig. 3C), and a signal value > 65,535 (Fig. 3D) ($p < 0.001$

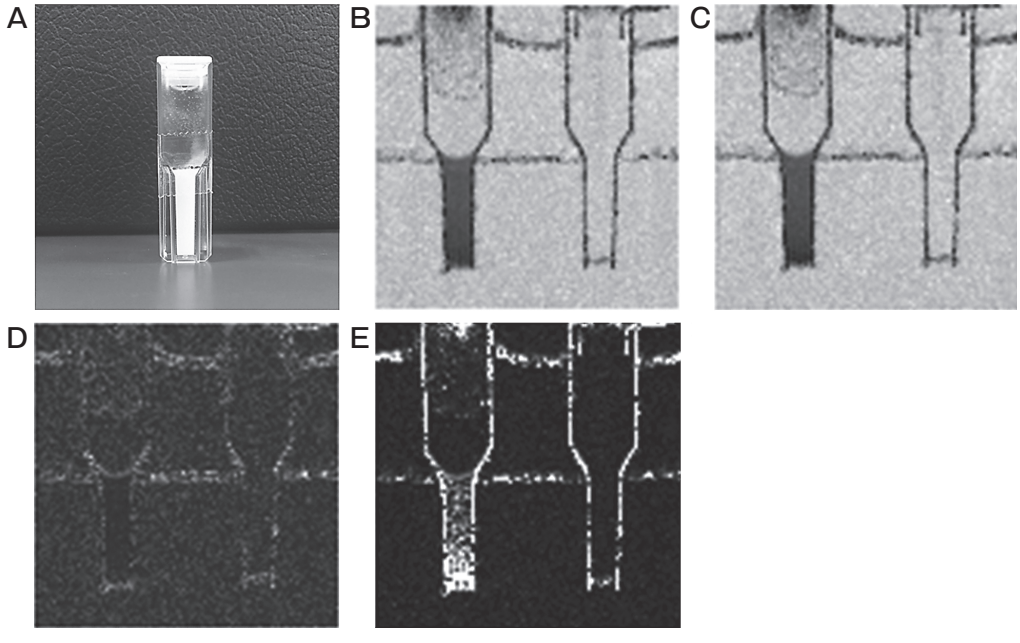

Fig. 2 Images obtained following the ADC subtraction method (ASM) calculation process. **A**, A bio-phantom was used as the validation sample; **B**, The 1st ADC map of the bio-phantom (*left side*) and physiological saline (*right side*), which was calculated using DWI with the readout segmentation of long variable echo-trains (RESOLVE)-basic sequence; **C**, The 2nd ADC map of the same bio-phantom and physiological saline, calculated using DWI with the RESOLVE-modify sequence; **D**, The image obtained following pixel subtraction with the absolute difference value between the 1st and 2nd ADC maps, which were converted from 16 to 32 bits and multiplied by the constant 10^{11}; **E**, The resultant ASM image is shown, which was obtained by dividing the image in panel (D) 3 times by the first ADC map and converted to 16 bits.

each). These results indicate that the ASM values in each pixel of the bio-phantom and physiological saline were calculated accurately, and thus that the ASM imaging software was able to visualize the ASM values correctly.

Discussion

We tested our new ASM imaging software for creating restricted diffusion images, and the verification of the ASM images clarified that this software program correctly obtains the ASM values of the bio-phantom and physiological saline, on a pixel-by-pixel basis.

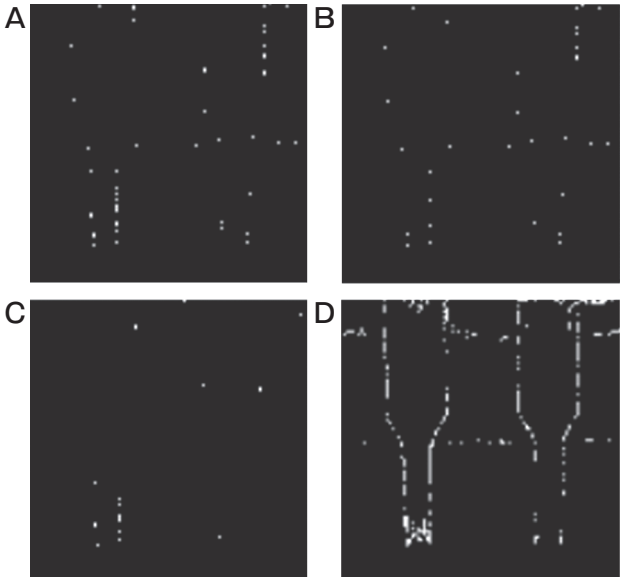

Fig. 3 Characteristic pixel values in the 32-bit ASM method; **A**, The *white* pixels with a signal value 0 in the ADC map; **B**, The *white* pixels with a value of infinity in the 32-bit ASM image; **C**, The *white* pixels with values Not a Number (NaN) in the 32-bit ASM image; **D**, The *white* pixels with a signal value >65,535 in the 32-bit ASM image. The numbers of pixels of infinity (B), NaN (C), and a signal value >65,535 (D) in 'bio-phantom and physiological saline' were low compared to those in 'plastic and air.' The ASM values in 'bio-phantom and physiological saline' were calculated accurately.

It has been reported that restricted diffusion imaging could be useful for diagnosis in clinic settings [11-17]. DKI is a representative imaging modality for restricted diffusion. DKI was reported to visualize lesions more sensitively than ADC maps [5, 6]. The new ASM imaging method, which provides images that are less distorted by using the RESOLVE-sequence, might become a new method for restricted diffusion imaging. The present report is the first concerning the creation and evaluation of ASM imaging software.

We used the free software from the U.S. NIH, *i.e.*, ImageJ, for the ASM imaging toward the goal of spreading the ASM method widely in future clinical research. ImageJ enables the conversion of gradients and inter-image calculations. ImageJ has already been used to analyze various research and medical images, including fundus photographs [18-25]. Macros and plugins are available to continuously and automatically perform several processes including inter-image calculations [18-23]. Plugins are faster than macros and are compatible with various operating systems [26], and several plugins have been developed and reported [18-23].

In the ASM image creation process, the appropriate selection of bits is required. Medical images such as MRI and CT are usually 16 bits. It is difficult to store and manage 32-bit images in medical systems, and these images are difficult to handle with general image processing software. As 32-bit images increase the data capacity compared to 16-bit images, they are not widely used in clinics. In the process of ASM calculation described herein, 32-bit images are used to remove the

Table 2 Comparison of the ratios of infinity, NaN, and >65,535 between the 'bio-phantom and physiological saline' and 'plastic and air' models

	Total pixel number	Pixel number (%)		
		Infinity	NaN	>65,535
Bio-phantom and physiological saline	6598	0 (0%)	0 (0%)	1 (0.02%)
Plastic and air	3203	31 (0.97%)	17 (0.53%)	299 (9.33%)
Statistics		$p<0.001$	$p<0.001$	$p<0.001$

NaN, Not a number. The significant difference in each ratio between "bio-phantom and physiological saline" and "plastic and air" was tested using Fisher's exact test. $p<0.05$ was determined as a significant difference.

limitations of 16 bits, but 32-bit images are converted to the final 16-bit ASM images so that they are suitable for medical systems.

When calculating with 32-bit images, care must be taken concerning the appearance of pixels with a signal value of infinity, NaN, or >65,535. In the 32-bit images, these three types of pixels matter during the conversion process of 32 bits to 16 bits. When an arbitrary signal value is divided by the signal value 0, the signal value becomes infinity. When the signal value 0 is divided by the signal value 0, the signal value obtained becomes NaN. When converting from 32 to 16 bits, the pixel value of infinity becomes 65,535, which is the maximum signal value of 16 bit-images, and the pixel value of NaN becomes 0. Therefore, if the first ADC map has a signal value of 0 (as indicated in Fig. 3A), the signal value in 32-bit ASM images become infinity (Fig. 3B) or NaN (Fig. 3C). These signal values are then converted into 65,535 or 0 as the final signal value in 16-bit ASM images. These values might affect the evaluation.

However, we observed pixels with a signal value of 0 (Fig. 3A), infinity (Fig. 3B) or NaN (Fig. 3C) in the plastic and air. Pixels with a signal value >65,535 were also observed in the plastic and air (Fig. 3D). No pixels in the bio-phantom or physiological saline had values of infinity or NaN, and few pixels in the bio-phantom and physiological saline had values of >65,535. These results indicated that 32-bit images could be converted to 16-bit images without affecting the ASM values of the bio-phantom. However, the results obtained through ASM should be interpreted cautiously, and we should take into account whether the subjects contain a signal value of 0, such as that found in the plastic and air.

Although medical images are usually DICOM (Digital Imaging and Communications in Medicine) images, ImageJ is unable to save images in the DICOM format during the ASM calculation process, and in the present study the images were saved in Tagged Image File Format (TIFF). Another image processing software is thus required to convert TIFF images to DICOM images for clinical use.

In recent years, the usefulness of restricted diffusion-weighted imaging modalities such as DKI has been reported. The ASM method is a new technique that can visualize restricted diffusion. To date, there is no ASM imaging software based on the ASM principle, and this is the first report concerning ASM imaging software. Our new ASM imaging software program might become available for clinical research on restricted diffusion-weighted imaging in the future.

Acknowledgments. We thank the staff of the Department of Radiology and the Central Division of Radiology of Okayama University Hospital for their support. This study was supported in part by Grants-in-Aid for Scientific Research (nos. C22591335, 15K09924 and 19K0809801) from the Ministry of Health, Labour and Welfare of Japan.

References

1. Lutsep HL, Albers GW, DeCrespigny A, Kamat GN, Marks MP and Moseley ME: Clinical utility of diffusion-weighted magnetic resonance imaging in the assessment of ischemic stroke. Ann Neurol (1997) 41: 574–580.
2. van Everdingen KJ, van der Grond J, Kappelle LJ, Ramos LMP and Mali WPTM: Diffusion-weighted magnetic resonance imaging in acute stroke. Stroke (1998) 29: 1783–1790.
3. Guo Y, Cai YQ, Cai ZL, Gao YG, An NY, Ma L, Mahankali S and Gao JH: Differentiation of clinically benign and malignant breast lesions using diffusion-weighted imaging. J Magn Reson Imaging (2002) 16: 172–178.
4. Tamada T, Sone T, Jo Y, Toshimitsu S, Yamashita T, Yamamoto A, Tanimoto D and Ito K: Apparent diffusion coefficient values in peripheral and transition zones of the prostate: comparison between normal and malignant prostatic tissues and correlation with histologic grade. J Magn Reson Imaging (2008) 28: 720–726.
5. Cao LK, Chen J, Duan T, Wang M, Jiang HY, Wei Y, Xia CC, Zhou XY, Yan X and Song B: Diffusion kurtosis imaging (DKI) of hepatocellular carcinoma: correlation with microvascular invasion and histologic grade. Quant Imaging Med Surg (2019) 9: 590–602.
6. Zhu LH, Zhang ZP, Wang FN, Cheng QH and Guo G: Diffusion kurtosis imaging of microstructural changes in brain tissue affected by acute ischemic stroke in different locations. Neural Regen Res (2019) 14: 272–279.
7. Yoshimura Y, Kuroda M, Sugianto I, Khasawneh A, Bamgbose BO, Hamada K, Barham M, Tekiki N, Kurozumi A, Matsushita T, Ohno S, Kanazawa S and Asaumi J: Development of a novel method for visualizing restricted diffusion using subtraction of apparent diffusion coefficient values. Mol Med Rep (2019) 20: 2963–2969.
8. Katashima K, Kuroda M, Ashida M, Sasaki T, Taguchi T, Matsuzaki H, Murakami J, Yanagi Y, Hisatomi M, Hara M, Kato H, Ohmura Y, Kobayashi T, Kanazawa S, Harada S, Takemoto M, Ohno S, Mimura S and Asaumi J: In vitro assessment of factors affecting the apparent diffusion coefficient of Jurkat cells using bio-phantoms. Acta Med Okayama (2013) 67: 359–367.
9. Yoshimura Y, Kuroda M, Sugianto I, Bamgbose BO, Miyahara K, Ohmura Y, Kurozumi A, Matsushita T, Ohno S, Kanazawa S and Asaumi J: The usefulness of readout-segmented echo-planar imaging (RESOLVE) for bio-phantom imaging using 3-tesla clinical MRI. Acta Med Okayama (2018) 72: 53–59.
10. John CR: Pixels; in The image processing handbook, 4th ed, Florida, CRC Press LLC. (2002) pp20–23.
11. Wan Q, Deng YS, Lei Q, Bao YY, Wang YZ, Zhou JX, Zou Q and Li XC: Differentiating between malignant and benign solid solitary pulmonary lesions: are intravoxel incoherent motion and diffusion kurtosis imaging superior to conventional diffusion-weighted

imaging? Eur Radiol (2019) 29: 1607–1615.
12. Huang Y, Lin Y, Hu W, Ma CC, Lin WX, Wang ZN, Liang JH, Ye W, Zhao JY and Wu RH: Diffusion kurtosis at 3.0T as an in vivo imaging marker for breast cancer characterization: correlation with prognostic factors. J Magn Reson Imaging (2019) 49: 845–856.
13. Taoka T, Fujioka M, Sakamoto M, Miyasaka T, Akashi T, Ochi T, Hori S, Uchikoshi M, Xu J and Kichikawa K: Time course of axial and radial diffusion kurtosis of white matter infarctions: period of pseudonormalization. AJNR Am J Neuroradiol (2014) 35: 1509–1514.
14. Raab P, Hattingen E, Franz K, Zanella FE and Lanfermann H: Cerebral gliomas: diffusional kurtosis imaging analysis of microstructural differences. Radiology (2010) 254: 876–881.
15. Hempel JM, Brendle C, Bender B, Bier G, Kraus MS, Skardelly M, Richter H, Eckert F, Schittenhelm J and Ernemann U: Diffusion kurtosis imaging histogram parameter metrics predicting survival in integrated molecular subtypes of diffuse glioma: an observational cohort study. Eur J Radiol (2019) 112: 144–152.
16. Yamada I, Sakamoto J, Kobayashi D, Miyasaka N, Wakana K, Oshima N, Wakabayashi A, Saida Y, Tateishi U and Eishi Y: Diffusion kurtosis imaging of endometrial carcinoma: correlation with histopathological findings. Magn Reson Imaging (2019) 57: 337–346
17. Zhao J, Wang YL, Li XB, Hu MS, Li ZH, Song YK, Wang JY, Tian YS, Liu DW and Yan X: Comparative analysis of the diffusion kurtosis imaging and diffusion tensor imaging in grading gliomas, predicting tumour cell proliferation and IDH-1 gene mutation status. J Neuro-Oncol (2019) 141: 195–203.
18. Schneider CA, Rasband WS and Eliceiri KW: NIH image to ImageJ: 25 years of image analysis. Nat Methods (2012) 9: 671–675.
19. Collins TJ: ImageJ for microscopy. Biotechniques (2007) 43: 25–30.
20. Feige JN, Sage D, Wahli W, Desvergne B and Gelman L: PixFRET, an ImageJ plug-in for FRET calculation that can accommodate variations in spectral bleed-throughs. Microsc Res Tech (2005) 68: 51–58.
21. Roszik J, Lisboa D, Szollosi J and Vereb G: Evaluation of intensity-based ratiometric FRET in image cytometry-approaches and a software solution. Cytom Part A (2009) 75A: 761–767.
22. Doube M, Kłosowski MM, Arganda-Carreras I, Cordelières FP, Dougherty RP, Jackson JS, Schmid B, Hutchinson JR and Shefelbine SJ: BoneJ: free and extensible bone image analysis in ImageJ. Bone (2010) 47: 1076–1079.
23. Fischer MJM, Uchida S and Messlinger K: Measurement of meningeal blood vessel diameter in vivo with a plug-in for ImageJ. Microvasc Res (2010) 80: 258–266.
24. Bonello L, Preda L, Conte G, Giannitto C, Raimondi S, Ansarin M, Maffini F, Summers P and Bellomi M: Squamous cell carcinoma of the oral cavity and oropharynx: what does the apparent diffusion coefficient tell us about its histology? Acta Radiol (2016) 57: 1344–1351.
25. Guo L, Tao J, Xia F, Yang Z, Ma X and Hua R: In vivo optical imaging of amblyopia: digital subtraction autofluorescence and split-spectrum amplitude-decorrelation angiography. Lasers Surg Med (2016) 48: 660–667.
26. Broeke J: Frameworks for macros and plugins; in Image processing with ImageJ, 2nd ed. Birmingham: Packt Publishing Ltd. (2015) pp129–138.